Statistica Sinica Preprint No: SS-2023-0184	
Title	Versatile Parametric Classes of Covariance Functions that Interlace Anisotropies and Hole Effects
Manuscript ID	SS-2023-0184
URL	http://www.stat.sinica.edu.tw/statistica/
DOI	10.5705/ss.202023.0184
Complete List of Authors	Alfredo Alegria and Xavier Emery
Corresponding Authors	Alfredo Alegria
E-mails	alfredo.alegria@usm.cl
Notice: Accepted version subject to English editing.	

Versatile Parametric Classes of Covariance Functions that Interlace Anisotropies and Hole Effects

Alfredo Alegría[1] and Xavier Emery[2,3]

[1] *Departamento de Matemática, Universidad Técnica Federico Santa María, Valparaíso, Chile*

[2] *Department of Mining Engineering, Universidad de Chile, Santiago, Chile*

[3] *Advanced Mining Technology Center, Universidad de Chile, Santiago, Chile*

Abstract: Covariance functions are a fundamental tool for modeling the dependence structure of spatial random fields. This work investigates novel constructions for covariance functions that enable the integration of anisotropies and hole effects in complex and versatile ways, having the potential to provide more accurate representations of dependence structures arising with real-world data. We show that these constructions extend widely used covariance models, including the Matérn, Cauchy, compactly-supported hypergeometric and cardinal sine models. We apply our results to a geophysical data set from a rock-carbonate aquifer and demonstrate that the proposed models yield more accurate predictions at unsampled locations compared to basic covariance models.

Key words and phrases: Nonmonotonic covariance models; Matérn covariance; Cauchy covariance; Gauss hypergeometric covariance; cardinal sine covariance; anisotropic random fields.

1. Introduction

Data indexed by spatial (hereafter, Euclidean) coordinates arise in many disciplines of the natural sciences, including climatology (Sang et al., 2011), oceanography (Wikle et al., 2013), environment (Rodrigues et al., 2015), ecology (Finley et al., 2011) and geosciences (Davis, 2002). Statistical and geostatistical models often assume the observed data to be a realization of a Gaussian random field, with the covariance function being the fundamental ingredient to capture the spatial dependence (Chilès and Delfiner, 2012), to understand the underlying spatial patterns and make reliable predictions.

Currently, there is a fairly extensive catalog of parametric families of stationary covariance functions that allow modeling a large number of patterns appearing in real situations, such as long-memory, hole effects, periodicities, degree of mean square differentiability, anisotropies, among others. Classical textbooks, such as Gaetan and Guyon (2010) and Chilès and Delfiner (2012), provide extensive insights into the wide range of available models. While existing models can handle many common patterns found in real data sets, some data sets may present complex combinations of features that require the development of new specialized models. In particular, anisotropies and hole effects are two common properties that can manifest on the covariance structure of data.

Anisotropy refers to the directional dependence of spatial data, where the level of association varies across different directions. We refer the reader to Chilès and Delfiner (2012), Allard et al. (2016) and Koch et al. (2020) for discussions on various types of anisotropy, including geometric, zonal, and product (componentwise) anisotropies. Hole effects, on the other hand, refer to the occurrence of negative covariance values at large distances, which can be attributed to the structured occurrence of high (low) values of a geo-referenced variable surrounded by low (high) values of this variable (Chilès and Delfiner, 2012). They can be explained by ecological (e.g., geographic competition, avoidance, attraction-repulsion, interaction, or aggregation), anthropogenic (e.g., land use, land management, soil tilling and cultivation), or geological (e.g., sedimentary, magmatic, diagenetic, migration, foliation, fracturing, faulting, or folding) processes. A typical example of hole effect takes place in the presence of a pseudo-periodicity in the spatial variability, which often arises along a specific direction, i.e., anisotropically.

To date, several hole effect models have been developed in the isotropic setting, such as pseudo periodic models (Christakos, 1984; Chilès and Delfiner, 2012; Hristopulos, 2015) and models with finitely many oscillations (Gaspari and Cohn, 1999; Gneiting, 2002; Vargas-Guzmán et al., 2002; Bellier and Monestiez, 2010; Alegría and Emery, 2024), for which the amplitude of

the hole effect is all the less pronounced as the space dimension increases (Chilès and Delfiner, 2012). However, the literature on anisotropic hole effect models is still sparse. Although some basic constructions that incorporate both anisotropy and hole effects can be designed easily (examples and references are provided in Section 2), more complex and sophisticated relationships may be required in practice. Our focus is on covariance models that feature both amenable expressions and interpretable parameters, and that are capable of achieving negative values of varying intensities depending on the spatial orientation. In particular, some models could display negative values only along specific spatial directions. We are motivated to study this type of models in order to have a flexible framework capable of capturing intricate dependence patterns present in real-world data, and enable more robust inference and prediction.

To accomplish this goal, we begin by examining the conditions under which the difference between two geometrically anisotropic stationary covariance functions is valid. In a purely isotropic setting, Ma (2005), Buhmann and Jäger (2020), Faouzi et al. (2020) and Posa (2023) utilized this methodology for constructing models with hole effects. Our findings thus expand upon these works by considering an anisotropic setting. Furthermore, we investigate an approach based on the difference between a merely

isotropic model and the average of shifted isotropic models. The shift direction is a critical element of this formulation, as it indicates the primary direction where the hole effect occurs. In addition, we study a construction that involves directional derivatives of a spatial random field; thus, a significant hole effect is expected in a predominant direction (directional derivative's sign can amplify the transitions between high and low values). We also investigate how the aforementioned constructions can be coupled with popular existing covariance models, such as the Matérn, Cauchy, compactly-supported hypergeometric and cardinal sine, to generalize these models to more versatile parametric functions.

The practical implications of this work will be explored through an application to a geophysical dataset. Our analysis will reveal that the proposed models lead to substantially improved predictions at unsampled locations in comparison with basic covariance models.

The article is organized as follows. Section 2 contains preliminary material on stationary spatial random fields, covariance functions and basic models that combine anisotropies and hole effects. Section 3 proposes general methodologies to construct models merging anisotropies and hole effects in a nontrivial manner. Section 4 offers explicit parametric families that use Matérn, Cauchy, compactly-supported hypergeometric and cardi-

nal sine models as a starting point. In Section 5, our findings are applied to a real data set. Section 6 presents conclusions and outlines potential avenues for future research. The online Supplementary Material provides an additional literature review on spatial hole effects, along with visual illustrations and simulation studies.

2. Preliminaries

Let $d \in \mathbb{N}$ and $\{Z(\boldsymbol{x}) : \boldsymbol{x} \in \mathbb{R}^d\}$ be a real-valued second-order zero-mean random field. The covariance function of such a field is the mapping $K : \mathbb{R}^d \times \mathbb{R}^d \to \mathbb{R}$ defined as $K(\boldsymbol{x}, \boldsymbol{x}') = \operatorname{cov}[Z(\boldsymbol{x}), Z(\boldsymbol{x}')]$. This is a positive semidefinite function, i.e., for all $n \in \mathbb{N}$, $v_1, \ldots, v_n \in \mathbb{R}$ and $\boldsymbol{x}_1, \ldots, \boldsymbol{x}_n \in \mathbb{R}^d$, $\sum_{i,j=1}^{n} v_i v_j K(\boldsymbol{x}_i, \boldsymbol{x}_j) \geq 0$. The mapping K is said to be stationary if there exists a function $C : \mathbb{R}^d \to \mathbb{R}$ such that $K(\boldsymbol{x}, \boldsymbol{x}') = C(\boldsymbol{x} - \boldsymbol{x}')$, for all $\boldsymbol{x}, \boldsymbol{x}' \in \mathbb{R}^d$. By abuse of language, C will be referred to as a stationary covariance function and we will say that C is positive semidefinite. Bochner's theorem (see, e.g., page 24 of Stein, 1999) provides a useful characterization of these mappings under an assumption of continuity: C is a continuous stationary covariance function if, and only if, it can be written as

$$C(\boldsymbol{h}) = \int_{\mathbb{R}^d} \exp\left(\imath \boldsymbol{h}^\top \boldsymbol{\omega}\right) F(\mathrm{d}\boldsymbol{\omega}), \qquad \boldsymbol{h} \in \mathbb{R}^d, \tag{2.1}$$

for some nonnegative, symmetric and finite measure F (called spectral measure) on $\mathbb{R}^d$ endowed with the Borel sigma-algebra, with $\imath$ standing for the imaginary unit. If F is absolutely continuous with respect to the Lebesgue measure, which happens if C is absolutely integrable, then $F(\mathrm{d}\boldsymbol{\omega}) = f(\boldsymbol{\omega})\mathrm{d}\boldsymbol{\omega}$, for some Lebesgue integrable function $f : \mathbb{R}^d \to \mathbb{R}$ known as the spectral density (Chilès and Delfiner, 2012, Section 2.3.3). In such a case, Fourier inversion yields

$$f(\boldsymbol{\omega}) = \frac{1}{(2\pi)^d} \int_{\mathbb{R}^d} \exp\left(-\imath \boldsymbol{\omega}^\top \boldsymbol{h}\right) C(\boldsymbol{h})\mathrm{d}\boldsymbol{h}, \qquad \boldsymbol{\omega} \in \mathbb{R}^d. \tag{2.2}$$

A stationary covariance function is said to be isotropic if there exists a function $\varphi : [0, \infty) \to \mathbb{R}$ such that $K(\boldsymbol{x}, \boldsymbol{x}') = \varphi(\|\boldsymbol{x} - \boldsymbol{x}'\|)$, for all $\boldsymbol{x}, \boldsymbol{x}' \in \mathbb{R}^d$, where $\|\cdot\|$ stands for the Euclidean norm on $\mathbb{R}^d$. The function φ is referred to as the radial part of K. We denote Φ_d the set of continuous functions φ that are the radial part of some isotropic covariance function in $\mathbb{R}^d \times \mathbb{R}^d$. Every member of Φ_d, for $d \geq 2$, can be written as the Hankel transform of order $(d-2)/2$ of a nonnegative bounded measure G_d on $[0, \infty)$ endowed with the Borel sigma-algebra (Schoenberg, 1938, Theorem 1), i.e.,

$$\varphi(h) = \int_0^\infty \Omega_d(hu)\mathrm{d}G_d(u), \qquad h \geq 0, \tag{2.3}$$

where $\Omega_d(s) = 2^{(d-2)/2}\Gamma(d/2)s^{-(d-2)/2}J_{(d-2)/2}(s)$, with Γ standing for the gamma function and J_ν for the Bessel function of the first kind of order

ν. If the spectral measure F is absolutely continuous with respect to the Lebesgue measure, then so is G_d. Furthermore, the spectral density f is a radial function and one has

$$\varphi(h) = (2\pi)^{d/2} h^{(2-d)/2} \int_0^\infty J_{(d-2)/2}(uh) f_d(u) u^{d/2} \mathrm{d}u, \qquad h \geq 0, \qquad (2.4)$$

and

$$f_d(u) = \frac{1}{(2\pi)^{d/2}} u^{(2-d)/2} \int_0^\infty J_{(d-2)/2}(uh) \varphi(h) h^{d/2} \mathrm{d}h, \qquad u \geq 0, \qquad (2.5)$$

where f_d is the radial part of f and will be referred to as the d-radial spectral density of φ (note that the expression (2.5) of this radial density depends on the space dimension d): $f(\boldsymbol{\omega}) = f_d(\|\boldsymbol{\omega}\|)$ for all $\boldsymbol{\omega} \in \mathbb{R}^d$.

As described in the introduction, the radial part φ of an isotropic covariance function can attain negative values at large distances, which is commonly referred to as a hole effect. For the sake of simplicity, suppose that $\int_0^\infty \mathrm{d}G_d(u) = 1$, then one has the following lower bound for the members of Φ_d: $\varphi(h) \geq \inf_{s \geq 0} \Omega_d(s)$. When $d = 2$ and $d = 3$, this lower bound is -0.403 and -0.218, respectively (Stein, 1999). As the spatial dimension d approaches infinity, the lower bound of the isotropic covariance function tends to zero, indicating that an isotropic hole effect becomes negligible with large spatial dimensions.

In the following sections, we aim to investigate parametric covariance

models that interlace anisotropy and hole effect. Note that some elementary constructions can be developed:

- Suppose that $\varphi \in \Phi_d$ has a hole effect, then $C(\boldsymbol{h}) = \varphi\left(\sqrt{\boldsymbol{h}^\top \mathbf{A} \boldsymbol{h}}\right)$ is a valid stationary covariance function, for any positive semidefinite matrix $\mathbf{A}$. This is one of the most utilized strategies to introduce anisotropy from an initial isotropic model, known as geometric (if $|\mathbf{A}| > 0$, with $|\cdot|$ denoting the determinant of a square matrix) or zonal (if $|\mathbf{A}| = 0$) anisotropy. Thus, hole effects and geometric/zonal anisotropies can coexist in a single family. However, this construction is overly rigid because the hole effect is constrained to occur in (almost) all directions with the same sharpness; of course, depending on the direction, the hole effect is attained at different ranges.

- Constructions of the form $C(\boldsymbol{h}) = \varphi_1(\|\boldsymbol{h}\|)\varphi_2(|h_i|)$, with $\varphi_1 \in \Phi_d$, $\varphi_2 \in \Phi_1$ and h_i being the ith element of $\boldsymbol{h}$, can exhibit hole effects in directions that are close to the i-th axis, provided that φ_2 has a hole effect. This approach also produces a pattern that is quite rigid, where the interval of negative values in all directions exhibiting a hole effect (primarily, in orientations approximately parallel to the i-th axis) has a similar length regardless of the direction considered. Variations of this construction include covariance functions of the form

$C(\boldsymbol{h}) = \varphi_1(|h_1|)\varphi_2(|h_2|)$ in the two-dimensional space, with $\varphi_1, \varphi_2 \in \Phi_1$ (one of them with a hole effect) (Thiébaux, 1976; Emery and Parra, 2013), or of the form $C(\boldsymbol{h}) = \varphi_1\left(\sqrt{\boldsymbol{h}^\top \mathbf{A}\boldsymbol{h}}\right)\varphi_2(|h_i|)$ with $\mathbf{A}$ a positive semidefinite matrix, $\varphi_1 \in \Phi_d$, and $\varphi_2 \in \Phi_1$ with a hole effect (Journel and Froidevaux, 1982; Le Blévec et al., 2018).

Figure S1 in Supplementary Material shows examples of these basic models, where the aforementioned structures can be seen. This work explores other constructions enabling complex combinations of these features.

3. General Results

3.1 Difference Between Geometrically Anisotropic Models

We will examine the conditions under which the difference between two geometrically anisotropic covariance functions remains positive semidefinite.

Proposition 1. *Let φ be a member of the class Φ_d possessing a d-radial spectral density f_d. Consider scalars $b_1, b_2 \geq 0$ and symmetric positive definite matrices $\mathbf{A}_1$ and $\mathbf{A}_2$. Thus,*

$$\mathcal{T}^{(1)}_{\mathbf{A}_1,\mathbf{A}_2,b_1,b_2}[\varphi](\boldsymbol{h}) = b_1\,\varphi\left(\sqrt{\boldsymbol{h}^\top \mathbf{A}_1\boldsymbol{h}}\right) - b_2\,\varphi\left(\sqrt{\boldsymbol{h}^\top \mathbf{A}_2\boldsymbol{h}}\right), \qquad \boldsymbol{h} \in \mathbb{R}^d, \tag{3.6}$$

is a stationary covariance function in $\mathbb{R}^d$ *if, and only if,*

$$b_1 \geq b_2 \frac{|\mathbf{A}_1|^{1/2}}{|\mathbf{A}_2|^{1/2}} \sup_{\boldsymbol{\omega}\in\mathbb{R}^d} \frac{f_d\left(\sqrt{\boldsymbol{\omega}^\top \mathbf{A}_2^{-1}\boldsymbol{\omega}}\right)}{f_d\left(\sqrt{\boldsymbol{\omega}^\top \mathbf{A}_1^{-1}\boldsymbol{\omega}}\right)}. \tag{3.7}$$

Proof 1. Based on Bochner's theorem, one must show that the inverse Fourier transform of (3.6), which is positively proportional to

$$b_1 \int_{\mathbb{R}^d} \exp\left(-\imath\boldsymbol{\omega}^\top \boldsymbol{h}\right) \varphi\left(\sqrt{\boldsymbol{h}^\top \mathbf{A}_1 \boldsymbol{h}}\right) \mathrm{d}\boldsymbol{h} - b_2 \int_{\mathbb{R}^d} \exp\left(-\imath\boldsymbol{\omega}^\top \boldsymbol{h}\right) \varphi\left(\sqrt{\boldsymbol{h}^\top \mathbf{A}_2 \boldsymbol{h}}\right) \mathrm{d}\boldsymbol{h}, \tag{3.8}$$

is nonnegative for every $\boldsymbol{\omega} \in \mathbb{R}^d$. A change of variable allows writing (3.8) in the following format:

$$\frac{b_1}{|\mathbf{A}_1|^{1/2}} \int_{\mathbb{R}^d} \exp\left(-\imath \left[\mathbf{A}_1^{-1/2}\boldsymbol{\omega}\right]^\top \boldsymbol{v}\right) \varphi\left(\sqrt{\boldsymbol{v}^\top \boldsymbol{v}}\right) \mathrm{d}\boldsymbol{v} - \frac{b_2}{|\mathbf{A}_2|^{1/2}} \int_{\mathbb{R}^d} \exp\left(-\imath \left[\mathbf{A}_2^{-1/2}\boldsymbol{\omega}\right]^\top \boldsymbol{v}\right) \varphi\left(\sqrt{\boldsymbol{v}^\top \boldsymbol{v}}\right) \mathrm{d}\boldsymbol{v}.$$

Thus, up to a positive factor, (3.8) can be written as

$$\frac{b_1}{|\mathbf{A}_1|^{1/2}} f_d\left(\sqrt{\boldsymbol{\omega}^\top \mathbf{A}_1^{-1}\boldsymbol{\omega}}\right) - \frac{b_2}{|\mathbf{A}_2|^{1/2}} f_d\left(\sqrt{\boldsymbol{\omega}^\top \mathbf{A}_2^{-1}\boldsymbol{\omega}}\right). \tag{3.9}$$

Finally, (3.9) is nonnegative for all $\boldsymbol{\omega} \in \mathbb{R}^d$ if, and only if, (3.7) holds. □

The negative term in (3.6) is the one that induces the hole effect, so matrix $\mathbf{A}_2$ is key to characterize the prevalent directions of the hole effect.

When the spectral density is radial and nonincreasing, the previous proposition can be simplified. Before stating the next result, we introduce the notation $\mathbf{A}_1 \succeq \mathbf{A}_2$ to indicate that $\mathbf{A}_1 - \mathbf{A}_2$ is positive semidefinite.

Corollary 1. *Suppose that φ belongs to Φ_d and has a nonincreasing d-radial spectral density f_d. Let $\mathbf{A}_1$ and $\mathbf{A}_2$ be positive definite matrices such that $\mathbf{A}_1 \succeq \mathbf{A}_2$, and $b_1, b_2 \geq 0$. Thus, (3.6) is a stationary covariance function in $\mathbb{R}^d$ if, and only if,*

$$b_1 \geq b_2 \frac{|\mathbf{A}_1|^{1/2}}{|\mathbf{A}_2|^{1/2}}. \tag{3.10}$$

Proof 2. Condition $\mathbf{A}_1 \succeq \mathbf{A}_2$ is equivalent to $\mathbf{A}_2^{-1} \succeq \mathbf{A}_1^{-1}$. Thus, $\boldsymbol{\omega}^\top \mathbf{A}_2^{-1} \boldsymbol{\omega} \geq \boldsymbol{\omega}^\top \mathbf{A}_1^{-1} \boldsymbol{\omega}$ for all $\boldsymbol{\omega} \in \mathbb{R}^d$. Since f_d is nonincreasing,

$$f_d\left(\sqrt{\boldsymbol{\omega}^\top \mathbf{A}_2^{-1} \boldsymbol{\omega}}\right) \leq f_d\left(\sqrt{\boldsymbol{\omega}^\top \mathbf{A}_1^{-1} \boldsymbol{\omega}}\right), \qquad \boldsymbol{\omega} \in \mathbb{R}^d.$$

Consequently, the supremum in the right hand side of (3.7) is identically equal to one (attained for $\boldsymbol{\omega} = \mathbf{0}$). □

Remark 1. A sufficient condition for the d-radial spectral density f_d to be nonincreasing is that φ belongs to Φ_{d+2} and possesses a $(d+2)$-radial spectral density f_{d+2}. Indeed, in such a case, φ is the Hankel transform of order $(d-2)/2$ of f_d, as per (2.4), and also the Hankel transform of order $d/2$ of f_{d+2}. This entails that f_d is the montée of order 2 of f_{d+2} (Matheron, 1965, formula I.4.8):

$$f_d(u) = 2\pi \int_u^\infty v f_{d+2}(v) \mathrm{d}v, \quad u \geq 0, \tag{3.11}$$

which is a nonincreasing function of u insofar as f_{d+2} is nonnegative.

The conditions in Corollary 1 can be stated in terms of the eigenvalues of $\mathbf{A}_1$ and $\mathbf{A}_2$. Let $\lambda_j(\mathbf{A}_i)$, $\lambda_{\min}(\mathbf{A}_i)$ and $\lambda_{\max}(\mathbf{A}_i)$ denote the j-th, minimum and maximum eigenvalues of $\mathbf{A}_i$, respectively, for $i = 1, 2$ and $j = 1, \ldots, d$.

Corollary 2. *Suppose that φ belongs to Φ_d and has a nonincreasing d-radial spectral density. Let $\mathbf{A}_1$ and $\mathbf{A}_2$ be positive definite matrices such that $\lambda_{\min}(\mathbf{A}_1) \geq \lambda_{\max}(\mathbf{A}_2)$, and $b_1, b_2 \geq 0$. Thus, (3.6) is a stationary covariance function in $\mathbb{R}^d$ if, and only if,*

$$b_1 \geq b_2 \left(\prod_{j=1}^{d} \frac{\lambda_j(\mathbf{A}_1)}{\lambda_j(\mathbf{A}_2)} \right)^{1/2}. \tag{3.12}$$

Remark 2. When $\mathbf{A}_i = a_i \mathbf{I}_d$, for $i = 1, 2$, with $a_1 \geq a_2$ and $\mathbf{I}_d$ being the $d \times d$ identity matrix, (3.6) reduces to the isotropic model

$$h \mapsto b_1 \, \varphi(\sqrt{a_1} h) - b_2 \, \varphi(\sqrt{a_2} h), \tag{3.13}$$

with $h = \|\boldsymbol{h}\| \geq 0$, and the respective validity condition (3.12) simplifies into

$$b_1 \geq b_2 \left(\frac{a_1}{a_2} \right)^{d/2}. \tag{3.14}$$

Our results align with prior literature concerning this topic in the purely isotropic case. Specifically, we recover Theorem 1(ii) in Ma (2005), and generalize Theorem 3.1 in Faouzi et al. (2020) and Corollaries 3-12 in Posa (2023). The results of this section can therefore be seen as an anisotropic

extension of previous literature related to the difference between isotropic covariance models (or nested models) and the so-called Zastavnyi operators.

3.2 Construction Based on Shifted Isotropic Models

We propose here an alternative approach for constructing anisotropic covariance functions that exhibit negative values in specific orientations. We start with an isotropic model of the form (3.13). Therefore, it becomes crucial to satisfy both condition (3.14) and the requirement of having a nonincreasing d-radial spectral density for φ to ensure that we start with an admissible covariance model. Then, we incorporate a shift in a determined direction to produce an anisotropic structure.

Proposition 2. *Let $\varphi \in \Phi_d$ and suppose that it has a nonincreasing d-radial spectral density. Consider constants $a_1, a_2 > 0$ and $b_1, b_2 \geq 0$ such that* (3.14) *holds. Thus, for all $\boldsymbol{\eta} \in \mathbb{R}^d$, the mapping*

$$\mathcal{T}^{(2)}_{a_1,a_2,b_1,b_2,\boldsymbol{\eta}}[\varphi](\boldsymbol{h}) = b_1\,\varphi\left(\sqrt{a_1}\|\boldsymbol{h}\|\right) - \frac{b_2}{2}\left[\varphi(\sqrt{a_2}\|\boldsymbol{h}-\boldsymbol{\eta}\|)+\varphi(\sqrt{a_2}\|\boldsymbol{h}+\boldsymbol{\eta}\|)\right], \quad \boldsymbol{h} \in \mathbb{R}^d, \tag{3.15}$$

is a stationary covariance function in $\mathbb{R}^d$.

Proof 3. Let $f_{a_i,d}$ denote the d-radial spectral density of $\varphi(\sqrt{a_i}h)$, for

$i = 1, 2$. Note that, for all $\boldsymbol{\omega} \in \mathbb{R}^d$, with $\omega = \|\boldsymbol{\omega}\|$,

$$\frac{1}{(2\pi)^d} \int_{\mathbb{R}^d} \exp\left(-\imath \boldsymbol{\omega}^\top \boldsymbol{h}\right) \varphi\left(\sqrt{a_2}\|\boldsymbol{h} - \boldsymbol{\eta}\|\right) \mathrm{d}\boldsymbol{h}$$
$$= \frac{1}{(2\pi)^d} \int_{\mathbb{R}^d} \exp\left(-\imath \boldsymbol{\omega}^\top [\boldsymbol{v} + \boldsymbol{\eta}]\right) \varphi\left(\sqrt{a_2}\|\boldsymbol{v}\|\right) \mathrm{d}\boldsymbol{v} = \exp\left(-\imath \boldsymbol{\omega}^\top \boldsymbol{\eta}\right) f_{a_2,d}(\omega).$$

Similarly, $(2\pi)^{-d} \int_{\mathbb{R}^d} \exp\left(-\imath \boldsymbol{\omega}^\top \boldsymbol{h}\right) \varphi\left(\sqrt{a_2}\|\boldsymbol{h} + \boldsymbol{\eta}\|\right) \mathrm{d}\boldsymbol{h} = \exp\left(\imath \boldsymbol{\omega}^\top \boldsymbol{\eta}\right) f_{a_2,d}(\omega)$.

Thus, for all $\boldsymbol{\omega} \in \mathbb{R}^d$, the inverse Fourier transform of (3.15) is

$$b_1 f_{a_1,d}(\omega) - \frac{b_2}{2}\left[\exp\left(-\imath \boldsymbol{\omega}^\top \boldsymbol{\eta}\right) f_{a_2,d}(\omega) + \exp\left(\imath \boldsymbol{\omega}^\top \boldsymbol{\eta}\right) f_{a_2,d}(\omega)\right]$$
$$= b_1 f_{a_1,d}(\omega) - b_2 \cos\left(\boldsymbol{\omega}^\top \boldsymbol{\eta}\right) f_{a_2,d}(\omega). \quad (3.16)$$

The right-hand side of (3.16) is lower-bounded by $b_1 f_{a_1,d}(\omega) - b_2 f_{a_2,d}(\omega)$, where the latter expression is the d-radial spectral density of (3.13). This quantity is non-negative as condition (3.14) is satisfied, i.e., (3.13) is positive semidefinite. The proof concludes invoking Bochner's theorem. □

The interest of the above proposition lies in the fact that all the isotropic constructions of the form (3.13) can be adapted according to (3.15) to produce anisotropic models. When the separation vector $\boldsymbol{h}$ is close to $\pm\boldsymbol{\eta}$, the negative part of (3.15) becomes predominant; thus, the hole effect is more significant in that direction.

Two limit cases of (3.15) are worth noting. On the one hand, as $\|\boldsymbol{\eta}\|$ approaches infinity, (3.15) tends to $b_1\, \varphi(\sqrt{a_1}h)$ (a rescaled version of the initial covariance model). On the other hand, when $\|\boldsymbol{\eta}\|$ approaches zero,

the nested model (3.13) is recovered. Thus, this construction can encompass purely isotropic models, both with and without hole effect, as special cases.

3.3 Models with Derivative Information

Our focus now turns to the study of anisotropic models whose construction incorporates directional derivatives of an isotropic random field. In contrast to previous strategies, this approach requires a covariance function twice differentiable at the origin as one of the initial ingredients, and no monotonicity conditions are required for the d-radial spectral density.

Proposition 3. *Let $\varphi_1, \varphi_2 \in \Phi_d$, with φ_2 being twice differentiable at the origin, and $\boldsymbol{u}$ be a unit vector in $\mathbb{R}^d$. Consider constants $a_1, a_2 > 0$ and $b_1, b_2 \geq 0$. Thus, the mapping*

$$\mathcal{T}^{(3)}_{a_1,a_2,b_1,b_2,\boldsymbol{u}}[\varphi_1,\varphi_2](\boldsymbol{h}) = b_1\varphi_1(\sqrt{a_1}\|\boldsymbol{h}\|) - b_2\Big[\cos^2(\theta(\boldsymbol{h},\boldsymbol{u}))\varphi_2''(\sqrt{a_2}\|\boldsymbol{h}\|) + \sin^2(\theta(\boldsymbol{h},\boldsymbol{u}))\frac{\varphi_2'(\sqrt{a_2}\|\boldsymbol{h}\|)}{\sqrt{a_2}\|\boldsymbol{h}\|}\Big], \quad (3.17)$$

where $\boldsymbol{h} \in \mathbb{R}^d$, with $\theta(\boldsymbol{h},\boldsymbol{u})$ being the angle between $\boldsymbol{h}$ and $\boldsymbol{u}$, is a stationary covariance function in $\mathbb{R}^d$.

Proof 4. Consider two independent zero-mean random fields on $\mathbb{R}^d$, denoted as Y_1 and Y_2, which possess covariance functions φ_1 and φ_2 in Φ_d,

respectively. Equation (5.29) in Chilès and Delfiner (2012) establishes that

$$\operatorname{cov}\left[\frac{\partial Y_2}{\partial \boldsymbol{u}}(\boldsymbol{x}), \frac{\partial Y_2}{\partial \boldsymbol{v}}(\boldsymbol{x}+\boldsymbol{h})\right] = -\frac{\left(\boldsymbol{h}^\top \boldsymbol{u}\right)^2}{\|\boldsymbol{h}\|^2}\left[\varphi_2''(\|\boldsymbol{h}\|) - \frac{\varphi_2'(\|\boldsymbol{h}\|)}{\|\boldsymbol{h}\|}\right] - \left(\boldsymbol{u}^\top \boldsymbol{v}\right)\frac{\varphi_2'(\|\boldsymbol{h}\|)}{\|\boldsymbol{h}\|},$$

for all $\boldsymbol{x}, \boldsymbol{h} \in \mathbb{R}^d$ and any pair of unit vectors $\boldsymbol{u}$ and $\boldsymbol{v}$ in $\mathbb{R}^d$, provided that φ_2 is twice differentiable at the origin. Thus, a direct calculation shows that the covariance function of the random field $\left\{(\partial Y_2/\partial \boldsymbol{u})(\boldsymbol{x}) : \boldsymbol{x} \in \mathbb{R}^d\right\}$ is given by $\boldsymbol{h} \mapsto -\cos^2(\theta(\boldsymbol{h}, \boldsymbol{u}))\varphi_2''(\|\boldsymbol{h}\|) - \sin^2(\theta(\boldsymbol{h}, \boldsymbol{u}))\varphi_2'(\|\boldsymbol{h}\|)/\|\boldsymbol{h}\|$. Based on previous calculations, one concludes that the covariance function of

$$Z(\boldsymbol{x}) = \sqrt{b_1} Y_1(\sqrt{a_1}\boldsymbol{x}) + \sqrt{\frac{b_2}{a_2}}\frac{\partial Y_2}{\partial \boldsymbol{u}}(\sqrt{a_2}\boldsymbol{x}), \qquad \boldsymbol{x} \in \mathbb{R}^d, \tag{3.18}$$

is given by (3.17), indicating that (3.17) is positive semidefinite. □

The rationale behind this approach is that the changes in sign of the directional derivative in (3.18) can accentuate the transitions between large and small values of the random field Z in a given direction; thus, marked hole effects in the orientation determined by $\boldsymbol{u}$ are expected. If $\boldsymbol{h}$ is approximately proportional to $\boldsymbol{u}$, the second-order derivative of φ_2 gains greater significance in (3.17). Conversely, if $\boldsymbol{h}$ is approximately orthogonal to $\boldsymbol{u}$, the term involving the first-order derivative becomes more dominant.

The parameters involved in this formulation do not require any elaborate restriction, as the positive semidefiniteness is inherently ensured by construction. A special case of (3.17) arises when setting $b_1 = 0$, where

the dominant component of the covariance structure is the term within brackets, representing the covariance function of the directional derivative of certain random field.

When the covariance functions of Y_1 and Y_2 are equal and given by $\varphi_1 = \varphi_2 := \varphi$, where φ is a function in Φ_d that is twice differentiable at the origin, we can conveniently denote the expression (3.17) as $\mathcal{T}^{(3)}_{a_1,a_2,b_1,b_2,\boldsymbol{u}}[\varphi]$.

Remark 3. In Proposition 3, one can substitute φ_1 with a stationary covariance model, which need not be isotropic. The validity of this alternative model is guaranteed by following the same proof as before. This slight variation offers enhanced flexibility in data modeling.

4. Explicit Parametric Families

4.1 Matérn, Cauchy and Hypergeometric Models

To provide concrete models derived from the previous findings, we introduce three commonly used parametric families of covariance functions: the Matérn, Cauchy and Gauss hypergeometric families.

1. The Matérn family of covariance functions is given by (Stein, 1999)

$$\mathcal{M}_\nu(t) = \frac{2^{1-\nu}}{\Gamma(\nu)} t^\nu \mathcal{K}_\nu(t), \qquad t \geq 0, \tag{4.19}$$

where $\mathcal{K}_\nu$ is the modified Bessel function of the second kind, with $\nu >$

0 being a shape parameter. The d-radial spectral density associated with this model, viewed as a function of $\omega = \|\boldsymbol{\omega}\|$, is given by $f_d^{\mathcal{M}}(\omega) = \pi^{-d/2}\left(\Gamma(\nu + d/2)/\Gamma(\nu)\right)(1+\omega^2)^{-\nu-d/2}$.

2. The Cauchy family of covariance functions is given by (see, e.g., Chilès and Delfiner, 2012)

$$\mathcal{C}_\delta(t) = (t^2+1)^{-\delta}, \qquad t \geq 0, \tag{4.20}$$

with $\delta > 0$ being a shape parameter. When $\delta > (d-1)/4$, its d-radial spectral density adopts the explicit form (Lim and Teo, 2009) $f_d^{\mathcal{C}}(\omega) = \pi^{-d/2}\left(2^{1-d/2-\delta}/\Gamma(\delta)\right)\omega^{-d/2+\delta}\mathcal{K}_{d/2-\delta}(\omega)$.

3. The Gauss hypergeometric family of covariance functions is given by (Emery and Alegría, 2022)

$$\mathcal{H}_{\alpha,\beta,\gamma}(t) = (1-t^2)_+^{\beta-\alpha+\gamma-d/2-1}\,{}_2F_1(\beta-\alpha, \gamma-\alpha; \beta-\alpha+\gamma-d/2; (1-t^2)_+), \qquad t \geq 0, \tag{4.21}$$

with ${}_2F_1$ denoting the Gauss hypergeometric function, $(\cdot)_+$ denoting the positive part and α, β, γ being shape parameters such that $2\alpha > d$, $2(\beta-\alpha)(\gamma-\alpha) \geq \alpha$ and $2(\beta+\gamma) \geq 6\alpha + 1$. Its d-radial spectral density is $f_d^{\mathcal{H}}(\omega) = \kappa(\alpha;\beta,\gamma)\,{}_1F_2(\alpha;\beta,\gamma;-\omega^2/2)$, with $\kappa(\alpha;\beta,\gamma)$ a positive factor and ${}_1F_2$ a generalized hypergeometric function. This

model encompasses the Euclid's hat (spherical), cubic, generalized Wendland and Askey covariances as particular cases.

Both $\mathcal{M}_\nu$ and $\mathcal{C}_\delta$ belong to Φ_d, for all $d \geq 1$, and both $f_d^{\mathcal{M}}$ and $f_d^{\mathcal{C}}$ are decreasing functions. As for $\mathcal{H}_{\alpha,\beta,\gamma}$, it belongs to Φ_{d+2} if $2\alpha > d+2$, $2(\beta-\alpha)(\gamma-\alpha) \geq \alpha$ and $2(\beta+\gamma) \geq 6\alpha+1$, in which case $f_d^{\mathcal{H}}$ is a nonincreasing function (recall Remark 1). Thus, these three models are in the range of applicability of Propositions 1 and 2.

While the Cauchy model is infinitely differentiable at the origin (Chilès and Delfiner, 2012), the Matérn and Gauss hypergeometric models are twice differentiable at the origin if, and only if, $\nu > 1$ (Stein, 1999) and $2\alpha > d+2$ (Emery and Alegría, 2022), respectively, and, in these cases, Proposition 3 can be applied.

In summary, we have the following corollaries.

Corollary 3. *Consider two positive definite matrices* $\mathbf{A}_1$ *and* $\mathbf{A}_2$ *such that* $\mathbf{A}_1 \succeq \mathbf{A}_2$*, and scalars* $b_1, b_2 \geq 0$*. Thus,* $\mathcal{T}^{(1)}_{\mathbf{A}_1,\mathbf{A}_2,b_1,b_2}[\mathcal{M}_\nu]$*,* $\mathcal{T}^{(1)}_{\mathbf{A}_1,\mathbf{A}_2,b_1,b_2}[\mathcal{C}_\delta]$ *and* $\mathcal{T}^{(1)}_{\mathbf{A}_1,\mathbf{A}_2,b_1,b_2}[\mathcal{H}_{\alpha,\beta,\gamma}]$*, with* $\nu > 0$*,* $\delta > (d-1)/4$*,* $2\alpha > d+2$*,* $2(\beta-\alpha)(\gamma-\alpha) \geq \alpha$ *and* $2(\beta+\gamma) \geq 6\alpha+1$*, are stationary covariance functions in* $\mathbb{R}^d$ *if, and only if, condition* (3.10) *holds.*

Corollary 4. *Let* $a_1, a_2 > 0$ *and* $b_1, b_2 \geq 0$ *satisfy condition* (3.14) *and* $\boldsymbol{\eta} \in \mathbb{R}^d$*. Thus,* $\mathcal{T}^{(2)}_{a_1,a_2,b_1,b_2,\boldsymbol{\eta}}[\mathcal{M}_\nu]$*,* $\mathcal{T}^{(2)}_{a_1,a_2,b_1,b_2,\boldsymbol{\eta}}[\mathcal{C}_\delta]$ *and* $\mathcal{T}^{(2)}_{a_1,a_2,b_1,b_2,\boldsymbol{\eta}}[\mathcal{H}_{\alpha,\beta,\gamma}]$*, with*

$\nu > 0$, $\delta > (d-1)/4$, $2\alpha > d+2$, $2(\beta-\alpha)(\gamma-\alpha) \geq \alpha$ and $2(\beta+\gamma) \geq 6\alpha+1$, are stationary covariance functions in $\mathbb{R}^d$.

Corollary 5. *Consider $a_1, a_2 > 0$ and $b_1, b_2 \geq 0$, and a unit vector $\boldsymbol{u} \in \mathbb{R}^d$. Thus, $\mathcal{T}^{(3)}_{a_1,a_2,b_1,b_2,\boldsymbol{u}}[\mathcal{M}_\nu]$ with $\nu > 1$, $\mathcal{T}^{(3)}_{a_1,a_2,b_1,b_2,\boldsymbol{u}}[\mathcal{C}_\delta]$ and $\mathcal{T}^{(3)}_{a_1,a_2,b_1,b_2,\boldsymbol{u}}[\mathcal{H}_{\alpha,\beta,\gamma}]$ with $2\alpha > d+2$, $2(\beta-\alpha)(\gamma-\alpha) \geq \alpha$ and $2(\beta+\gamma) \geq 6\alpha+1$, are stationary covariance functions in $\mathbb{R}^d$.*

In order to exhibit the versatility of the proposed models, we provide visual illustrations in Supplementary Material (see Figure S2).

4.2 Cardinal Sine Model

Our focus now turns to the cardinal sine (or wave) covariance function, defined through

$$\mathcal{W}(t) = \frac{\sin(t)}{t}, \qquad t > 0, \tag{4.22}$$

and $\mathcal{W}(0) = 1$. This model belongs to Φ_d, for $d \leq 3$. When $d = 3$, this model does not possess a spectral density. However, for $d \leq 2$, one has (Arroyo and Emery, 2021)

$$f_d^{\mathcal{W}}(\omega) = \frac{1}{2\pi^{(d-1)/2}\Gamma((3+d)/2)}(1-\omega^2)_+^{(1-d)/2}, \qquad \omega \geq 0. \tag{4.23}$$

In particular, when $d = 2$ and $0 \leq \omega < 1$, (4.23) is an increasing mapping. As a result, Propositions 1 and 2 are not applicable to this model. The

conditions of Proposition 3, on the other hand, can be readily verified for $d \leq 3$, leading to the subsequent corollary.

Corollary 6. *Let $d \leq 3$. Consider $a_1, a_2 > 0$ and $b_1, b_2 \geq 0$, and a unit vector $\boldsymbol{u} \in \mathbb{R}^d$. Thus, $\mathcal{T}^{(3)}_{a_1,a_2,b_1,b_2,\boldsymbol{u}}[\mathcal{W}]$ is a stationary covariance function in $\mathbb{R}^d$.*

Recall that Proposition 3 offers the flexibility to combine models from different parametric families. As an example, we can consider $\mathcal{T}^{(3)}_{a_1,a_2,b_1,b_2,\boldsymbol{u}}[\mathcal{M}_\nu, \mathcal{W}]$, which constitutes a valid stationary covariance model for dimensions $d \leq 3$.

Figure S3 in Supplementary Material shows examples of $\mathcal{T}^{(3)}_{a_1,a_2,b_1,b_2,\boldsymbol{u}}[\mathcal{W}]$ and $\mathcal{T}^{(3)}_{a_1,a_2,b_1,b_2,\boldsymbol{u}}[\mathcal{M}_{1/2}, \mathcal{W}]$ for specific parametric settings.

5. Real Data Analysis

We now present an application of our models in groundwater hydrology. We consider a geophysical data set from a carbonate-rock shallow aquifer located in Martin county, south Florida, and documented in Parra et al. (2006, 2009). Such shallow aquifers are an essential resource of groundwater, and their petrophysical and hydraulic properties (such as hydraulic conductivity, transmissivity, specific storage, specific yield, and porosity) need to be specified accurately to understand the groundwater storage and recharge potentials, to forecast the quantity of available water, and to op-

timally plan groundwater pumping from wells penetrating the aquifer.

In the aquifer under consideration, the porosity and other properties have been directly measured along wells that sample the aquifer but are widely spaced, with a sampling mesh of several hundred meters. To complement these measurements, cross-well reflection seismic surveys have been conducted to measure the P-wave impedance, a variable that strongly correlates with porosity and is therefore helpful for mapping the aquifer properties, delineating its lateral heterogeneities, and assessing the fluid paths (Parra and Emery, 2013; Emery and Parra, 2013). The P-wave impedance was calculated by means of a band-limited inversion algorithm (Olderburg et al., 1983; Parra et al., 2009) that integrates the petrophysical and geophysical well log data and the cross-well reflection data, leading to an image of the subsurface with a better vertical resolution and reduced artifacts in comparison to traditional seismic travel-time tomography (Beydoun et al., 1988). The result is a cross-section of an interwell region in a depth interval of 270 feet (approx. 82.3 m), with a vertical resolution of 0.61 m (2 feet) and a horizontal resolution of 3.05 m (10 feet), totaling 17,145 observations.

To reduce the number of data, we employ for our analysis a spatial resolution of 20 feet and 4 feet in the horizontal and vertical coordinates, respectively, which leads to a set of 4352 impedance data. Also, to remove

the trend in the east coordinate and improve the description of the data by a stationary random field model, we utilize a smoothing spline approach. The estimated trend exhibits a distinct pattern, gradually transitioning from high to low values as one moves from west to east. In Figure 1, one can observe the original data, the fitted trend, the residuals, and the corresponding histogram. These residuals can be interpreted as the realization of a stationary zero-mean Gaussian random field. We randomly select and exclude 400 observations of the dataset (approximately 10% of the observations) for posterior validation purposes, while the remaining observations constitute the training set.

A significant hole effect is present in the vertical direction. It can be explained by the presence of major geological structures, corresponding to permeability barriers alternating vertically with high-porosity structures. The former are characterized by tight limestone and isolated vugs, whereas the latter are associated with interconnected matrix and vugs or with a combination of interconnected vugs surrounded by limestone (Parra et al., 2009). Cyclic behaviors in the vertical covariances or variograms of rock properties are often observed in carbonate sequences and can be explained by periodic processes of deposition due to eustatic sea level oscillations or to tectonic activities (Chilès and Delfiner, 2012; Le Blévec et al., 2020).

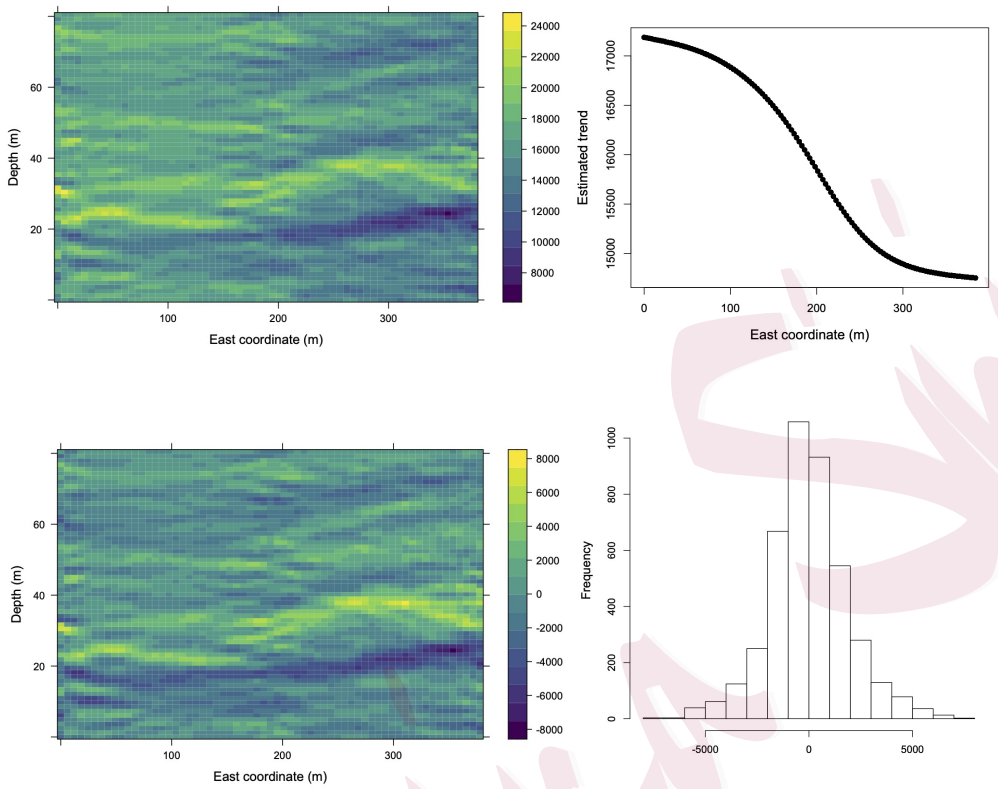

Figure 1: From top left to bottom right: original data set of impedance, fitted trend in the east direction, residuals and the corresponding histogram. The east and depth are shifted to a local coordinate system.

Taking into account this marked axial pattern, characterized by dissimilar scales along the east and depth coordinates, we consider:

I. A model of the form $C_1(\boldsymbol{h}; \sigma^2, a_1, a_2) = \sigma^2 \exp(-a_1\|\boldsymbol{h}\|)\mathcal{W}(a_2|h_2|)$.

II. A model of the form $C_2(\boldsymbol{h}; \sigma^2, a_1, a_2) = \sigma^2 \exp(-a_1\|\boldsymbol{h}\|)\cos(a_2|h_2|)$.

III. A convex combination of isotropic and zonal anisotropic covariances

$$C_3(\boldsymbol{h};\sigma^2,a_1,a_2,\omega,\boldsymbol{v}) = \sigma^2\left[\omega\exp(-a_1\|\boldsymbol{h}\|) + (1-\omega)\exp\left(-a_2|\boldsymbol{v}^\top\boldsymbol{h}|\right)\cos\left(a_2|\boldsymbol{v}^\top\boldsymbol{h}|\right)\right],$$

where $\omega \in [0,1]$ and $\boldsymbol{v}$ is a 2-dimensional unit vector, which is parameterized in terms of its polar angle θ.

IV. We use Model I as a building block and then incorporate derivative information using Proposition 3. The resulting model adopts the form $C(\boldsymbol{h};\sigma^2,a_1,a_2,a_3) = (3/4)\left[C_1(\boldsymbol{h};\sigma^2,a_1,a_2) + C_{\text{derivative}}(\boldsymbol{h};\sigma^2,a_3)\right]$, where

$$C_{\text{derivative}}(\boldsymbol{h};\sigma^2,a_3) = \sigma^2\left[\cos^2(\theta(\boldsymbol{h},\boldsymbol{u}))\varphi''(\sqrt{a_3}\|\boldsymbol{h}\|) + \sin^2(\theta(\boldsymbol{h},\boldsymbol{u}))\frac{\varphi'(\sqrt{a_3}\|\boldsymbol{h}\|)}{\sqrt{a_3}\|\boldsymbol{h}\|}\right],$$

with $\boldsymbol{u} = [0,1]^\top$ fixed and φ of the form (4.22). This model is an example of the variant described in Remark 3.

For each model, σ^2, a_1 and a_2 are positive parameters. In Model IV, $a_3 > 0$ is an additional scale parameter. Models I and II are constructed through a multiplicative combination of an isotropic exponential covariance and a covariance with an oscillating behavior along the second axis; in particular, Model II is an example of the *multiplicative composite* models studied in Journel and Froidevaux (1982). These formulations result in models characterized by a damped structure, with a pronounced hole effect, especially along the second axis. On the other hand, Model III is a weighted linear

combination of an isotropic exponential model and a damped model that depends on a hyperplane of change (zonal anisotropy). The reason for this additive combination is that real phenomena usually deviate from a pure zonal model (Allard et al., 2016). Model IV is a more sophisticated version of Model I, incorporating derivative information, as explained above.

For each model, we estimate the parameters through a composite likelihood (CL) method based on differences (Curriero and Lele, 1999; Varin et al., 2011). Table 1 shows the CL estimates together with the value of the objective function at the optimum. For comparison purposes, we also fit a modified version of Model IV using an automated least squares (LS) procedure instead of the CL method. For this strategy, we set $\sigma^2 = 4 \times 10^6$, $a_1 = 0.135$, $a_2 = 0.818$ and $a_3 = 0.067$, in order to obtain a model that matches the structural features of the directional empirical variograms. Figure 2 shows the fitted variogram models I, IV and IV (LS) along three spatial orientations (to avoid overloading the figures, we include plots only for the models that demonstrate the best predictive performances in the concluding part of this section). By construction, Model IV that is based on the LS method presents a more accurate description of the empirical variograms, but a poorer log-CL value (Table 1). On the contrary, Models I and IV that are based on the CL method do not perfectly match the empirical

Table 1: Parameters and log-CL of fitted covariance models.

Model	$\widehat{\sigma}^2$	$\widehat{a}_1$	$\widehat{a}_2$	$\widehat{a}_3$	$\widehat{\theta}$	$\widehat{\omega}$	log-CL
I	4.036×10^6	1.105×10^{-2}	0.717	–	–	–	−13,165,439
II	3.835×10^6	4.918×10^{-2}	0.265	–	–	–	−13,179,245
III	4.188×10^6	8.663×10^{-2}	0.195	–	1.585	0.175	− 13,160,480
IV	4.062×10^6	3.299×10^{-3}	0.526	2.441	–	–	−13,165,205
IV (LS)	4×10^6	0.135	0.818	0.067	–	–	−13,188,178

variograms, a situation that is commonly encountered in practice. Interestingly, Model III exhibits a good fit, which can be explained by the fact that it has more parameters. The estimated angle $\widehat{\theta}$ gives rise to a hyperplane of change with estimated vector $\widehat{\boldsymbol{v}} = [-0.014, 0.999]^\top$. In other words, the estimation captures the pronounced axial pattern exhibited by the data. To obtain a more comprehensive visualization of the fitted models, Figure 3 displays a global plot of the covariances.

To enhance our analysis, we conduct a split-sample study for model validation, with the 400 data that have been left out of the model fitting. We apply simple kriging using each model and evaluate the prediction accuracy using metrics such as the root mean square error (RMSE) and mean absolute error (MAE). Among the models that were tested, Model IV fitted with the CL method demonstrates a clear advantage, with the RMSE and MAE reduced by 10% to 19% with respect to the closest competitors

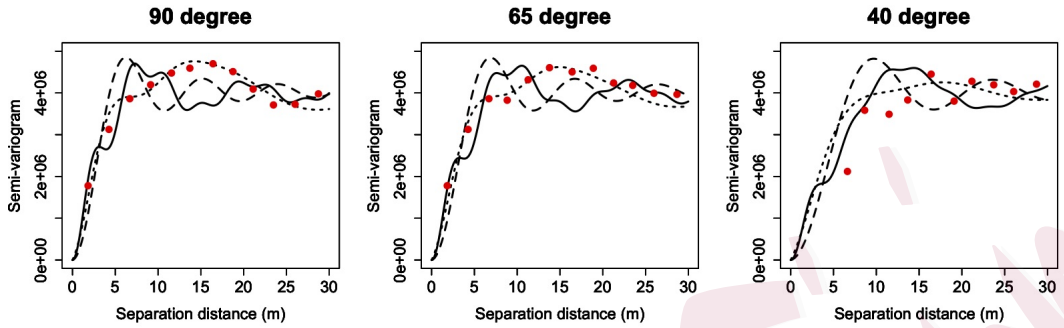

Figure 2: Empirical (red circles) and modeled (lines) directional variograms of impedance along directions dipping 90° (left), 65° (center) and 40° (right). Dashed line: Model I fitted through CL; Solid line: Model IV fitted through CL; Dotted line: Model IV fitted through LS.

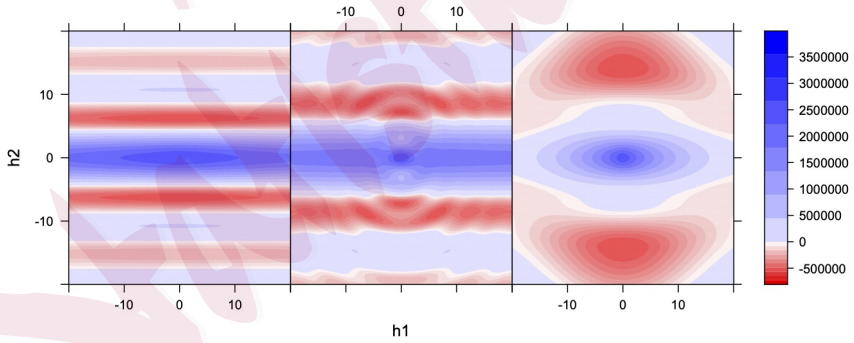

Figure 3: From left to right: Model I fitted through CL, Model IV fitted through CL and Model IV fitted through LS.

on our list (see Table 2). In Figure 4 (left panel), boxplots showing the absolute errors of the best three models are presented. Model IV based on CL outperforms the other models in terms of prediction accuracy. This superiority is evident through reduced quartiles and upper whisker. To gain insight into the dispersion of prediction errors, Figure 4 (right panel) compares the actual versus predicted values in the validation study, based on Model IV fitted through the CL method.

Table 2: Cross-validation scores: root mean square error (RMSE) and mean absolute error (MAE).

	Model				
	I	II	III	IV	IV (LS)
RMSE	741.55	850.01	960.03	662.27	767.04
MAE	546.12	634.12	756.89	457.97	564.76

As a summary of this study, we emphasize the importance of (i) identifying a hole effect in the spatial correlation structure of regionalized data, (ii) interpreting it in the light of the physics of the phenomenon under study (in the present case, geological cycles along the vertical direction), and (iii) accurately modeling such an effect, with likelihood-based techniques in preference to least-square strategies. Our results offer an enhanced versatility with respect to existing hole effect covariance models, together with some parsimony that favors the estimation of the parameters.

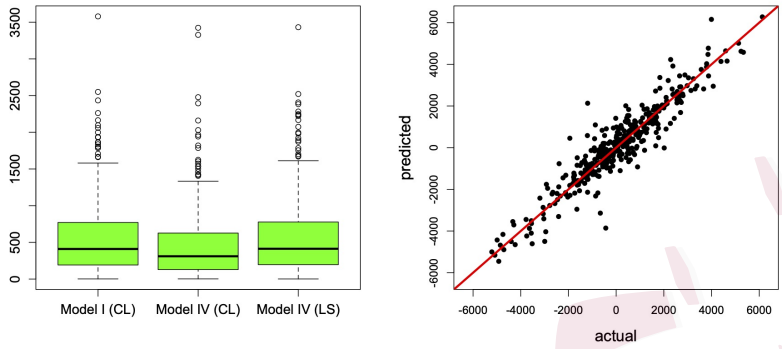

Figure 4: (Left) Comparison of absolute prediction errors among the covariance models. (Right) Comparison of actual versus predicted values in the cross-validation study, based on Model IV fitted through the CL method.

6. Conclusions

This work aimed to design new covariance models with complex characteristics. We restricted our attention to models that combine anisotropies and hole effects, and illustrated their practical impact with an application to a geophysical data set. We believe that the pursuit of increasingly flexible models, while maintaining a certain level of simplicity and parsimony, is an area that should continue to be explored. Some recent ideas in this direction can be found in Fuglstad et al. (2015), Alegria et al. (2021), Ma and Bhadra (2023) and Berild and Fuglstad (2023), among others.

We illustrated the use of the proposed constructions with well-established

families of covariance functions, although our formulations have the potential to be effectively combined with many other parametric families, such as the powered exponential or the hyperbolic models, among others. In particular, employing compactly-supported covariances (such as the Gauss hypergeometric covariance) as a starting point provides models that lead to sparse covariance matrices with quite distinctive structures, allowing for computationally efficient inference (Kaufman et al., 2008), prediction (Furrer et al., 2006) and simulation (Dietrich and Newsam, 1993) techniques.

Extending these results to the multivariate setting, where several coregionalized variables are jointly analyzed and the covariance functions are matrix-valued, presents an interesting area of exploration, albeit accompanied by significant challenges, as the model complexity intensifies due to the rapid growth in the number of parameters and the intricate restrictions imposed among them to ensure positive semidefiniteness.

Supplementary Material

The online supplement complements the article with additional material. Section S1 offers a comprehensive literature review on spatial hole effects. Section S2 contains figures that illustrate both basic and versatile covariance models. In Section S3, a simulation study reinforces the discussion within

the manuscript regarding the flexibility of covariance models.

Acknowledgements

This work was partially funded by the National Agency for Research and Development of Chile (ANID), through grants ANID Fondecyt 1210050 (AA and XE) and ANID PIA AFB230001 (XE), as well as by Universidad Técnica Federico Santa María, through grant Proyectos Internos USM 2023 PI_LIR_23_11 (AA).

References

Alegría, A. and Emery, X. (2024). Matrix-valued isotropic covariance functions with local extrema. *Journal of Multivariate Analysis*, 200:105250.

Alegria, A., Emery, X., and Porcu, E. (2021). Bivariate Matérn covariances with cross-dimple for modeling coregionalized variables. *Spatial Statistics*, 41:100491.

Allard, D., Senoussi, R., and Porcu, E. (2016). Anisotropy models for spatial data. *Mathematical Geosciences*, 48:305–328.

Arroyo, D. and Emery, X. (2021). Algorithm 1013: An R implementation of a continuous spectral algorithm for simulating vector Gaussian random

fields in Euclidean spaces. *ACM Transactions on Mathematical Software*, 47(1):8.

Bellier, E. and Monestiez, P. (2010). A spatial covariance model with a single wave effect and a finite range. *Statistics and Probability Letters*, 80:1343–1347.

Berild, M. O. and Fuglstad, G.-A. (2023). Spatially varying anisotropy for Gaussian random fields in three-dimensional space. *Spatial Statistics*, 55:100750.

Beydoun, W., Delvaux, J., Mendes, M., Noual, G., and Tarantola, A. (1988). Practical aspects of an elastic migration/inversion of crosshole data for reservoir characterization: A Paris Basin example. *Geophysics*, 54(12):1587—-1595.

Buhmann, M. and Jäger, J. (2020). Multiply monotone functions for radial basis function interpolation: Extensions and new kernels. *Journal of Approximation Theory*, 256:105434.

Chilès, J.-P. and Delfiner, P. (2012). *Geostatistics: Modeling Spatial Uncertainty*. John Wiley & Sons.

Christakos, G. (1984). On the problem of permissible covariance and variogram models. *Water Resources Research*, 20(2):251—265.

Curriero, F. C. and Lele, S. (1999). A composite likelihood approach to semivariogram estimation. *Journal of Agricultural, Biological and Environmental Statistics*, 4(1):9–28.

Davis, J. (2002). *Statistics and Data Analysis in Geology*. John Wiley & Sons.

Dietrich, C. and Newsam, G. (1993). A fast and exact method for multidimensional Gaussian stochastic simulations. *Water Resources Research*, 19:2961–2969.

Emery, X. and Alegría, A. (2022). The Gauss hypergeometric covariance kernel for modeling second-order stationary random fields in Euclidean spaces: Its compact support, properties and spectral representation. *Stochastic Environmental Research and Risk Assessment*, 36:2819—2834.

Emery, X. and Parra, J. (2013). Integration of crosswell seismic data for simulating porosity in a heterogeneous carbonate aquifer. *Journal of Applied Geophysics*, 98:254–264.

Faouzi, T., Porcu, E., Bevilacqua, M., and Kondrashuk, I. (2020). Zastavnyi

operators and positive definite radial functions. *Statistics & Probability Letters*, 157:108620.

Finley, A. O., Banerjee, S., and MacFarlane, D. W. (2011). A hierarchical model for quantifying forest variables over large heterogeneous landscapes with uncertain forest areas. *Journal of the American Statistical Association*, 106(493):31–48.

Fuglstad, G.-A., Lindgren, F., Simpson, D., and Rue, H. (2015). Exploring a new class of non-stationary spatial Gaussian random fields with varying local anisotropy. *Statistica Sinica*, 25(1):115–133.

Furrer, R., Genton, M. G., and Nychka, D. (2006). Covariance tapering for interpolation of large spatial datasets. *Journal of Computational and Graphical Statistics*, 15(3):502–523.

Gaetan, C. and Guyon, X. (2010). *Spatial Statistics and Modeling*, volume 90. Springer.

Gaspari, G. and Cohn, S. (1999). Construction of correlation functions in two and three dimensions. *Quarterly Journal of the Royal Meteorological Society*, 125(554):723—-757.

Gneiting, T. (2002). Compactly supported correlation functions. *Journal of Multivariate Analysis*, 83(2):493—508.

Hristopulos, D. T. (2015). Covariance functions motivated by spatial random field models with local interactions. *Stochastic Environmental Research and Risk Assessment*, 29:739–754.

Journel, A. and Froidevaux, R. (1982). Anisotropic hole-effect modeling. *Mathematical Geology*, 14(3):217–239.

Kaufman, C. G., Schervish, M. J., and Nychka, D. W. (2008). Covariance tapering for likelihood-based estimation in large spatial data sets. *Journal of the American Statistical Association*, 103(484):1545–1555.

Koch, D., Lele, S., and Lewis, M. A. (2020). Computationally simple anisotropic lattice covariograms. *Environmental and Ecological Statistics*, 27(4):665–688.

Le Blévec, T., Dubrule, O., John, C. M., and Hampson, G. J. (2018). Geostatistical modelling of cyclic and rhythmic facies architectures. *Mathematical Geosciences*, 50:609–637.

Le Blévec, T., Dubrule, O., John, C. M., and Hampson, G. J. (2020).

Geostatistical earth modeling of cyclic depositional facies and diagenesis. *AAPG Bulletin*, 104(3):711–734.

Lim, S. and Teo, L. P. (2009). Gaussian fields and Gaussian sheets with generalized Cauchy covariance structure. *Stochastic Processes and Their Applications*, 119(4):1325–1356.

Ma, C. (2005). Linear combinations of space-time covariance functions and variograms. *IEEE transactions on signal processing*, 53(3):857–864.

Ma, P. and Bhadra, A. (2023). Beyond Matérn: On a class of interpretable confluent hypergeometric covariance functions. *Journal of the American Statistical Association*, 118(543):2045–2058.

Matheron, G. (1965). *Les Variables Régionalisées et Leur Estimation*. Masson, Paris.

Olderburg, D., Scheuer, T., and Levy, S. (1983). Recovery of the acoustic impedance from reflection seismograms. *Geophysics*, 48(10):1318—-1337.

Parra, J. and Emery, X. (2013). Geostatistics applied to cross-well reflection seismic for imaging carbonate aquifers. *Journal of Applied Geophysics*, 92:68–75.

Parra, J., Hackert, C., and Bennett, W. (2006). Permeability and porosity

images based on P-wave surface seismic data: Application to a South Florida aquifer. *Water Resources Research*, 42(2):W02415.

Parra, J., Hackert, C., Richardson, E., and Clayton, N. (2009). Porosity and permeability images based on crosswell seismic measurements integrated with FMI logs at the Port Mayaca aquifer, South Florida. *The Leading Edge*, 28(10):1212–1219.

Posa, D. (2023). Special classes of isotropic covariance functions. *Stochastic Environmental Research and Risk Assessment*, 37:1615–1633.

Rodrigues, E. R., Gamerman, D., Tarumoto, M. H., and Tzintzun, G. (2015). A non-homogeneous poisson model with spatial anisotropy applied to ozone data from Mexico city. *Environmental and Ecological Statistics*, 22:393–422.

Sang, H., Jun, M., and Huang, J. Z. (2011). Covariance approximation for large multivariate spatial data sets with an application to multiple climate model errors. *The Annals of Applied Statistics*, 5(4):2519–2548.

Schoenberg, I. J. (1938). Metric spaces and completely monotone functions. *Annals of Mathematics*, 39(4):811–841.

Stein, M. L. (1999). *Statistical Interpolation of Spatial Data: Some Theory for Kriging*. Springer, New York.

Thiébaux, H. (1976). Anisotropic correlation functions for objective analysis. *Monthly Weather Review*, 104:994—1002.

Vargas-Guzmán, J., Warrick, A., and Myers, D. (2002). Coregionalization by linear combination of nonorthogonal components. *Mathematical Geology*, 34(4):405—419.

Varin, C., Reid, N., and Firth, D. (2011). An overview of composite likelihood methods. *Statistica Sinica*, 21(1):5–42.

Wikle, C. K., Milliff, R. F., Herbei, R., and Leeds, W. B. (2013). Modern statistical methods in oceanography: A hierarchical perspective. *Statistical Science*, 28(4):466–486.